communications physics

ARTICLE

https://doi.org/10.1038/s42005-023-01194-0 OPEN

Charge transfer driving interfacial reconstructions in perovskite oxide heterostructures

Yao Li[1,2,4], Pengxiang Hou[2,4], Zhongnan Xi[2], Yeming Xu[2], Yiren Liu[2], Hao Tian[2,3], Jiayi Li[2], Yurong Yang[2✉], Yu Deng[2] & Di Wu[2✉]

Charge transfer in perovskite oxide heterostructures could break the delicate balance among charge, spin, orbital and lattice order at the interface, producing exotic phenomena that cannot be observed in bulk materials. Here, opposite interfacial charge transfer directions are observed in $SrIrO_3/NdNiO_3$ and $SrIrO_3/LaNiO_3$ 3*d*/5*d* perovskite heterostructures. This is accompanied with an inverse change of Ni e_g orbital polarization and Ni-O *pd* hybridization across the interface, by stretching/compressing the out-of-plane Ni-O bond in the opposite internal electrical field due to the opposite electron transfer direction. These interfacial reconstructions finally bring about a manipulation on the transport and magnetic characteristics. This work reveals that A site cation in perovskite heterostructures could be a knob to control the interfacial charge transfer direction, and the 3*d*/5*d* perovskite interfaces are excellent platform to study the complex interplay between various order parameters and stimulate novel interfacial effects.

[1] Institute for Advanced Materials, Hubei Normal University, Huangshi 435002, China. [2] National Laboratory of Solid State Microstructures, Collaborative Innovation Center of Advanced Microstructures, Jiangsu Key Laboratory of Artificial Functional Materials, and Department of Materials Science and Engineering, Nanjing University, Nanjing 210093, China. [3] School of Physics and Electronic Engineering, Zhengzhou Normal University, Zhengzhou 450044, China. [4] These authors contributed equally: Yao Li, Pengxiang Hou. ✉email: yangyr@nju.edu.cn; diwu@nju.edu.cn

The interplay between charge, spin, orbital and lattice order parameters at perovskite oxide interfaces could produce abundant physical phenomena and provide concepts for novel electric and magnetic devices, such as high-mobility electron gas at the interface between insulator $SrTiO_3$ and $LaAlO_3$[1], exchange bias in heterostructures consisting of paramagnetic $LaNiO_3$ and ferromagnetic $LaMnO_3$[2], long-range Josephson coupling in superconducting $YBa_2Cu_3O_7$ layers across ferromagnetic $La_{0.7}Sr_{0.3}MnO_3$[3]. Among various interfacial effects, charge transfer is a common but important one. Generally, charge transfer occurs due to the discontinuity of polarity, valence and Fermi level across the interface[4]. Specific charge transfer might be achieved by artificially designing the hetero-interface[5], which could play an important role on electronic structures[6,7] and/or even lattice parameters[8,9]. This kind of interfacial reconstruction provides a handle to tune the delicate coexistence of various quantum phases and profound competitions among various ground states with different macroscopic transport and magnetic properties.

For decades, 3*d* transition metal oxides have been intensively studied for interfacial charge transfer, including perovskite nickelates[7,10]. Since magnetic and transport characteristics of nickelates are closely related to the valence state of Ni cations and the Ni–O *pd* hybridization[11,12], the interfacial charge transfer has been used to manipulate the metal-insulator transition, the magnetic structures and the charge ordered phase in nickelate heterostructures. Besides 3*d* transition metal oxides, the interfacial charge transfer in 5*d* transition metal oxides based heterostructures has recently attracted much attention, where the spin-orbit coupling is strong enough to compete with the electron correlation and might produce novel physical properties that cannot be observed in 3*d* heterostructures. In $SrIrO_3/SrRuO_3$ heterostructures, electrons are transferred from $SrIrO_3$ to $SrRuO_3$, bring about a persistent metallicity even in a single $SrIrO_3$ layer[13]. In $SrMnO_3/SrIrO_3$ superlattices, driven by interfacial electron transfer from Ir^{4+} to Mn^{4+}, ferromagnetic order and anomalous Hall effect appear, associated with strong spin-orbit coupling[14]. Charge transfer has also been observed at the interface of nickelates and iridates. For example, Liu et al. reported high spin state for both Ir and Ni cations in $SrIrO_3/LaNiO_3$ superlattices and explained the unusual magnetism of Ir^{5+} in terms of a charge transfer enhanced crystal field overwhelming the spin-orbit coupling[15]. Wen et al. also observed a change in the transport characteristics in $Sr_2IrO_4/LaNiO_3$ heterojunctions due to charge transfer and electronic reconstruction at the interface[16].

Although nickelates often act as electron acceptor in heterostructures, an abnormal increase of Ni valence has been observed in $LaNiO_3/SrIrO_3$ heterostructures[17]. To further explore the charge transfer across iridate/nickelate interfaces, a playground for the competition between electron correlation and spin-orbit coupling, here, we fabricated $SrIrO_3/NdNiO_3$ (SIO/NNO) and $SrIrO_3/LaNiO_3$ (SIO/LNO) heterostructures by pulsed laser deposition and comparatively studied their characters. An opposite interfacial charge transfer together with an opposite e_g orbital polarization are observed in these two heterostructures, leading to different transport and magnetic characteristics. With the help of X-ray absorption spectroscopy (XAS), X-ray photoelectron spectroscopy (XPS) and scanning transmission electron microscopy (STEM), the observations are discussed in terms of reconstructions of interfacial Ni–O bond and *pd* hybridization due to the electron transfer induced local electric fields, which are in opposite directions in the two heterostructures. The emergent magnetism in SIO/LNO, which is absent in SIO/NNO, is ascribed to the unusual Ni^{4+} cations, as a result of interfacial charge transfer.

Results and discussion

Hereafter, the SIO/NNO and SIO/LNO superlattices are labeled as $[SIO_2/NNO_k]_l$ and $[SIO_2/LNO_k]_l$, with k the thickness of NNO and LNO in unit cells (u.c.), l the number of superlattice periods, respectively. Unless otherwise stated, all the superlattices were kept at 24 u.c. in thickness, i.e., $(2 + k)\cdot l = 24$.

Structural characterization. Reflective high energy electron diffraction (RHEED) oscillations recorded during deposition of the $[SIO_2/NNO_2]_6$ and $[SIO_2/LNO_2]_6$ superlattices are shown in Supplementary Fig. 1. The periodic oscillations and streaky RHEED patterns observed indicates a layer-by-layer growth, which enables to achieve the heterostructures as designed. To check the heterostructures, X-ray diffraction (XRD) $\theta - 2\theta$ scans around the (001) diffraction peak of the $SrTiO_3$ (STO) substrate were performed. Figure 1a, b shows XRD patterns of the $[SIO_2/NNO_k]_l$ and $[SIO_2/LNO_k]_l$ superlattices, respectively, with various nickelate thickness and periodic repetitions. The numbers above the peaks indicate the *i*th satellite peak. The appearance of the satellite peaks indicates the periodically modulated superstructures, i.e., well-defined superlattices, have been achieved. The modulation period thickness can be calculated from the relation $\Lambda = \lambda/(2\Delta\theta \cdot \cos\theta_B)$, where λ is the X-ray wavelength, $\Delta\theta$ stands for radian distance between two adjacent satellite peaks, and θ_B is the Bragg diffraction angle. The experimental thickness of superlattice period Λ_{exp} thus calculated are 16.37, 25.34, 34.16, and 60.44 Å for $[SIO_2/NNO_k]_l$ with $k = 2$, 4, 6, and 10, respectively, and 16.03, 23.11, 31.43, and 56.12 Å for $[SIO_2/LNO_k]_l$ with $k = 2$, 4, 6, and 10, respectively. The total thickness of the superlattices can be obtained by $t = \lambda/(2\Delta\alpha\cdot\cos\theta_B)$, where $\Delta\alpha$ stands for radian distance between two adjacent thickness fringes. Thus, the actual number of periods in the superlattices can be calculated by t/Λ_{exp}. As shown in the insets of Fig. 1a, b, the measured numbers of period are plotted as functions of the nominal ones for both $[SIO_2/NNO_k]_l$ and $[SIO_2/LNO_k]_l$ superlattice with $l = 2$, 3, 4 and 6. All data points are close to the line through the origin with slope = 1, indicating the periodic structures close to those designed. Figure 1c, d shows the X-ray reciprocal space mappings of $[SIO_2/NNO_{10}]_2$ and $[SIO_2/LNO_{10}]_2$ superlattices around the STO (103) reflection. The superlattices share the same in-plane reciprocal vector with the substrate, indicating a fully strained state. All the superlattice samples show a smooth surface in step-terrace morphology. The root-mean-square roughness, acquired over an area of 3 μm × 3 μm, is below 165 pm. Figure 1e, f shows surface atomic force microscope (AFM) images of the $[SIO_2/NNO_2]_6$ and $[SIO_2/LNO_2]_6$ superlattice, for example. Figure 1g, h displays the height profile along the blue line indicates the step is about 4.0 Å in height, in agreement with that of a perovskite unit cell.

Interfacial charge transfer. Figure 2a, b shows Ni L_3-edge XAS of SIO_2/NNO_{10} and SIO_2/LNO_{10} bilayers in comparison with that of 10 u.c.-thick NNO (NNO_{10}) and LNO (LNO_{10}) thin film. The Ni L_3 absorption spectra of the NNO_{10} and LNO_{10} film exhibit a single peak at about 853.3 eV, in agreement with those reported in the literature for Ni^{3+} cations at about 853.5 eV[18–20]. The absorption peak energy of the SIO_2/NNO_{10} bilayer is 0.2 eV lower than that of the NNO_{10} film, indicating a reduced Ni valence and a transfer of electron from Ir to Ni in the SIO_2/NNO_{10} bilayer. Contrary to the SIO_2/NNO_{10} bilayer, the absorption peak energy of the SIO_2/LNO_{10} bilayer shifts by 0.4 eV toward higher energy from that of the LNO_{10} film. This indicates an increased Ni valence and a transfer of electron from Ni to Ir in the SIO_2/LNO_{10} bilayer. Although Ni^{2+} is frequently reported in nickelate

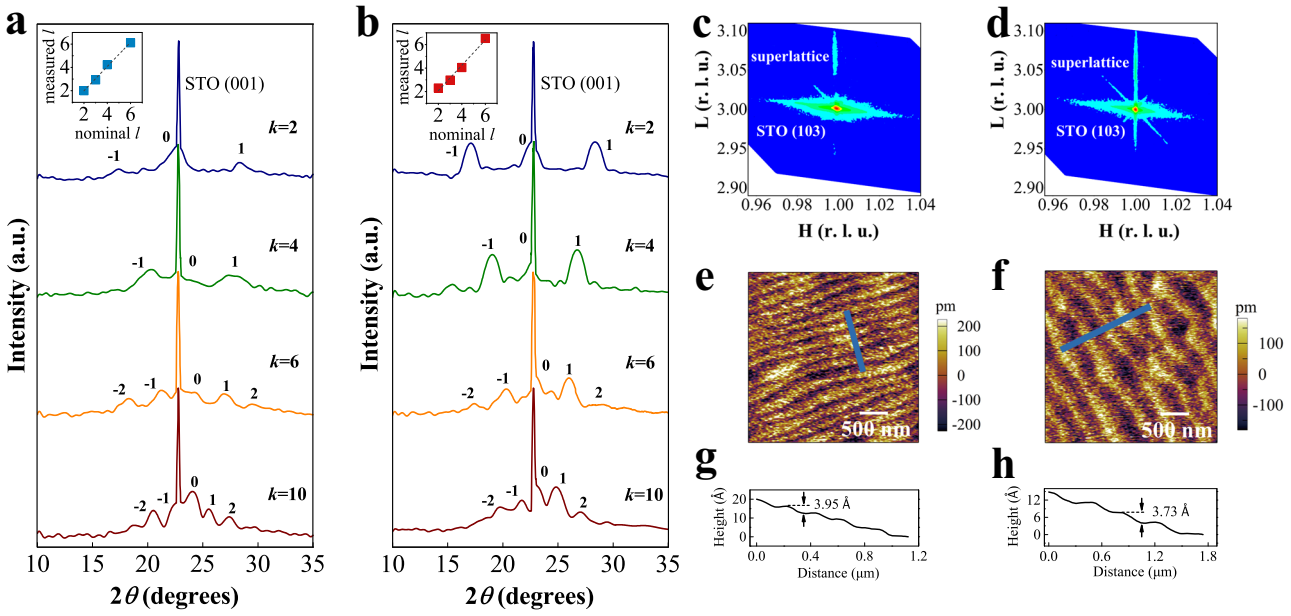

Fig. 1 Structural characterizations. X-ray diffraction patterns of **a** $[(SrIrO_3)_2/(NdNiO_3)_k]_l$ and **b** $[(SrIrO_3)_2/(LaNiO_3)_k]_l$ superlattices ($k = 2$, 4, 6, 10) deposited on (001) $SrTiO_3$ (STO) substrates. The numbers above the patterns indicate the ith satellite peaks. The insets in **a** and **b** show the measured numbers of period plotted as functions of the nominal ones. Reciprocal space mappings of **c** $[(SrIrO_3)_2/(NdNiO_3)_{10}]_2$ and **d** $[(SrIrO_3)_2/(LaNiO_3)_{10}]_2$ superlattices around the STO (103) reflection. The atomic force microscope images of the **e** $[(SrIrO_3)_2/(NdNiO_3)_2]_6$ and **f** $[(SrIrO_3)_2/(LaNiO_3)_2]_6$ sample surface, respectively. **g**, **h** The corresponding height profiles along the blue lines on the atomic force microscope images of **e** and **f**, where the step height is obtained as 3.95 and 3.73 Å, respectively.

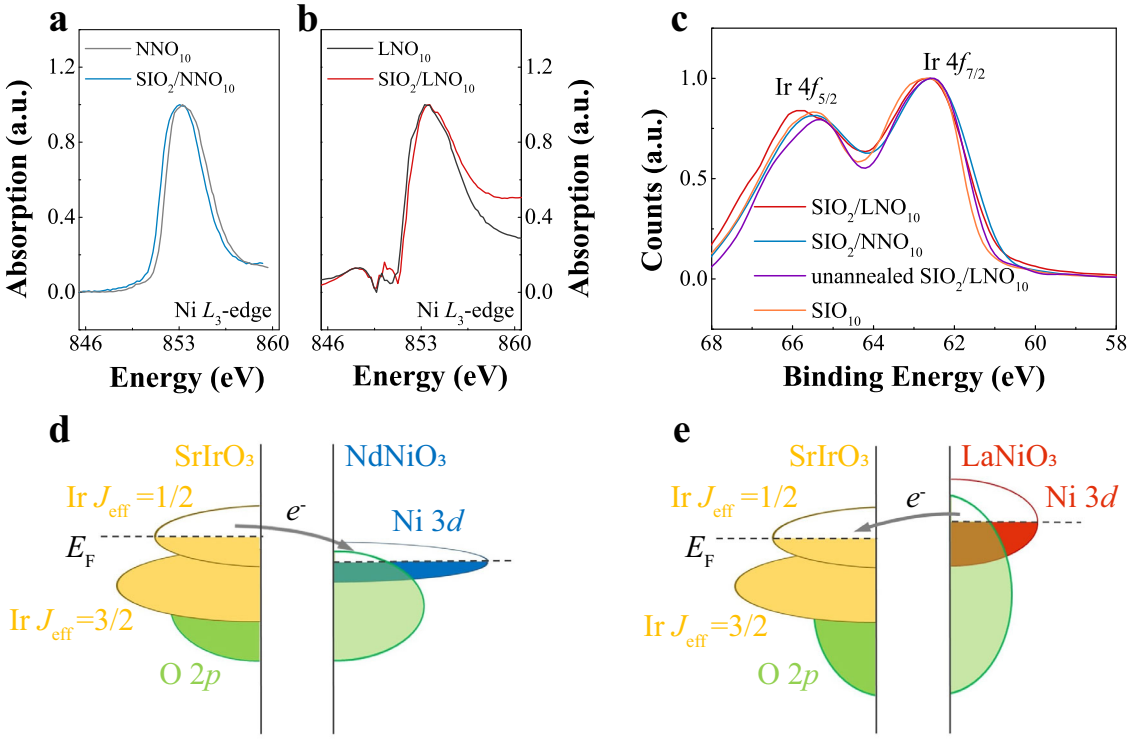

Fig. 2 Interfacial electron transfer. Ni L_3-edge X-ray absorption spectra (XAS) of **a** $(SrIrO_3)_2/(NdNiO_3)_{10}$ bilayer (blue line), abbreviated as SIO_2/NNO_{10} and **b** $(SrIrO_3)_2/(LaNiO_3)_{10}$ bilayer (red line), abbreviated as SIO_2/LNO_{10}, in comparison with those of NNO_{10} (gray line) and LNO_{10} (black line) thin films. The La M_4-edge from the LNO components is fitted with Gaussian-Lorentzian functions and subtracted. **c** Ir 4f core level X-ray photoelectron spectra (XPS) of SIO_2/NNO_{10} (blue line) and SIO_2/LNO_{10} (red line) bilayers in comparison with those of SIO_{10} (yellow line) thin film and SIO_2/LNO_{10} bilayer unannealed in oxygen (purple line). Schematic density of states of **d** SIO and NNO, **e** SIO and LNO across the interface.

heterostructures due to interfacial charge transfer[7,10,21], Ni^{4+} is less stable and rarely observed. Recently, Wang et al. reported that Ni^{4+} cations could be stabilized in $SrNiO_3/LaFeO_3$ superlattices with desired $LaFeO_3$ thickness[22]. Yamagami et al. also reported a low-spin Ni^{4+} state in sulfur-coordinated Ni complexes, as revealed by XAS[23].

To further investigate the charge transfer across the SIO_2/NNO_{10} and SIO_2/LNO_{10} interfaces, XPS of Ir 4*f* core level in SIO_2/NNO_{10} and SIO_2/LNO_{10} bilayers are measured, as shown in Fig. 2c, in comparison with those in a SIO_2/LNO_{10} bilayer without oxygen annealing and in a 10 u.c.-thick SIO (SIO_{10}) thin film. Banerjee et al. has reported that the Ir $4f_{5/2}$ and $4f_{7/2}$ spin-orbital split decreases as the Ir valence increases, for example, 3.1 eV in Ir_2O_3 and 2.7 eV in IrO_2[24]. It is advantageous to evaluate Ir valence using this spin-orbital split because possible surface charge effect, which prevents determining the binding energy precisely, can be avoided. The Ir 4*f* spin-orbital split in SIO_2/NNO_{10}, SIO_{10}, SIO_2/LNO_{10} is 2.8, 2.9, and 3.2 eV, respectively, indicating that the Ir valence in the SIO_2/NNO_{10} (SIO_2/LNO_{10}) bilayer is higher (lower) than that in the SIO_{10} thin film. The Ir 4*f* spin-orbital split in the deliberately unannealed SIO_2/LNO_{10} bilayer is 2.7 eV, indicating an even higher Ir valence, which will be discussed later. The results of Ir 4*f* XPS are consistent with the XAS of Ni L_3-edge, demonstrating the opposite electron transfer direction across the SIO_2/NNO_{10} and SIO_2/LNO_{10} interfaces, i.e., from Ir to Ni in the former but from Ni to Ir in the latter. The A-site cations in perovskite nickelates can be a knob to switch the electron transfer direction across the iridate/nickelate interface.

Charge transfer as functions of the nickelate thickness in $[SIO_2/NNO_k]_l$ and $[SIO_2/LNO_k]_l$ superlattices was studied. As shown in Supplementary Fig. 2, the energy shift of Ni *L*-edge absorption peak decreases with increasing nickelate thickness *k* in both superlattices. Since the energy shift of absorption peak corresponds to the average valence of Ni, this is reasonable that the transferred charges are constrained at the interfaces rather than distributed across the whole nickelate layers. Chien et al. has also reported that the charge transfer occurred only within 1 or 2 u.c. at the interface[25].

In perovskite nickelates, the O 2*p* band lies very close to, or even above the Ni 3*d* band to produce a strong *pd* hybridization, making it necessary to describe the electronic states of nickelates with a mixture of $3d^7$ and $3d^8\underline{L}$ states $|\psi\rangle = \alpha\,|3d^7\rangle + \beta\,|3d^8\underline{L}\rangle$ ($\alpha^2 + \beta^2 = 1$), where $\underline{L}$ stands for an oxygen hole, the degree of covalence is given by the ratio β^2/α^2[26]. Based on this, we may ascribe the opposite interfacial electron transfer across the SIO_2/NNO_{10} and SIO_2/LNO_{10} interfaces to the difference in the band structure of NNO and LNO[5]. Due to the smaller ionic radius of Nd, the Ni–O–Ni bond angle in bulk NNO is 157°, smaller than the 165° Ni–O–Ni bond angle in bulk LNO, while the Ni–O bond length is 1.940 Å in bulk NNO, larger than the 1.935 Å Ni–O bond length in bulk LNO[27]. These structural differences result in a weaker Ni–O *pd* hybridization, i.e., narrower O 2*p* and Ni 3*d* bands and less $3d^8\underline{L}$ component (smaller β) in NNO. The work function of nickelates could be represented as $\phi_{Ni} - \beta^2\,|\Delta|$, where ϕ_{Ni} is the electron affinities of Ni, Δ is the charge transfer energy[26]. Therefore, the Fermi level of NNO is lower and the work function of NNO is larger than those of LNO[28,29]. The opposite electron transfer direction observed above can be understood as long as the work function of SIO lies in between the Fermi levels of NNO and LNO, as schematically shown in Fig. 2d, e. There is evidence that perovskite nickelates may be negative charge transfer compounds, where the Ni electronic state could be represented as $|\psi\rangle = \alpha\,|3d^7\rangle + \beta\,|3d^8\underline{L}^n\rangle$[30]. In this case, the observed opposite charge transfer could still be explained in line with the above scenario.

Orbital polarization and *pd* hybridization. Interfacial electron transfer in perovskite heterostructures have been reported to able to modify the band filling[7] or change the crystal fields felt by the Ni cations at the octahedron center[9], leading to an orbital reconstruction. We then measure the e_g orbital polarization in SIO/NNO and SIO/LNO heterostructures, evaluated by XAS acquired with the incident beam linearly polarized in (I_σ) and out (I_π) of the film plane. Figure 3a, b shows normalized Ni L_3-edge XAS of SIO_2/NNO_{10} and SIO_2/LNO_{10} bilayers, respectively, and corresponding X-ray linear dichroism (XLD) spectra, defined as the differential XAS intensity measured with I_π and I_σ ($I_\pi - I_\sigma$). Supplementary Fig. 3a, b shows the XAS and XLD of NNO_{10} and LNO_{10} thin films, respectively, for comparison. I_σ (I_π) photons preferentially excite Ni 2*p* electrons into the empty Ni $d_{x^2-y^2}$ ($d_{3z^2-r^2}$) orbital. Therefore, the larger absorption intensity represents lower occupation and higher energy of the orbital. It is clear from Supplementary Fig. 3a, b that $d_{x^2-y^2}$ is preferentially occupied than $d_{3z^2-r^2}$ in the NNO_{10} film while the two e_g orbitals are nearly degenerate in the LNO_{10} film, in agreement with previous reports[18]. For example, Tung et al. observed a preferential occupation of the $d_{x^2-y^2}$ orbital in NNO thin films deposited on $SrTiO_3$ substrates and explained it by tensile strain induced distortion of the NiO_6 octahedra[18]. However, Chakhalian et al. reported that in LNO thin films, the rotation of the NiO_6 octahedra produces an additional breathing distortion that makes the two e_g orbitals degenerate even when the lattice is tetragonally distorted[19]. It is interesting that in the SIO_2/NNO_{10} bilayer, the $d_{3z^2-r^2}$ orbital is preferentially occupied, contrary to that in the NNO_{10} thin film, as indicated by the stronger absorption of I_σ. While in the SIO_2/LNO_{10} bilayer, the two e_g orbitals are no longer degenerate as in the LNO_{10} thin film and the electrons preferentially occupy the $d_{x^2-y^2}$ orbital. The opposite electron transfer direction in the SIO_2/NNO_{10} and SIO_2/NNO_{10} bilayers is accompanied by an opposite orbital polarization in the Ni e_g orbitals. It is well known that the energy of the e_g orbitals in perovskite nickelates is associated with the corresponding Ni–O bond length and the shorter the in-plane (out-of-plane) bond length, the higher the $d_{x^2-y^2}$ ($d_{3z^2-r^2}$) energy[18,31,32]. Since all the nickelate heterostructures and thin films in this work are fully strained to the STO substrates, the in-plane Ni–O bond length is the same in all the samples. The opposite orbital polarization observed can be ascribed to the reconstruction of the out-of-plane Ni–O bonds. The preferential occupation of the $d_{3z^2-r^2}$ orbital observed in the SIO_2/NNO_{10} bilayer, where Ni accepts electrons transferred from Ir, is similar to the $LaTiO_3/LaNiO_3$ interface reported, where a transfer of electron from Ti to Ni across the interface produces a local electric field, stretches the out-of-plane Ni–O bond and decreases the $d_{3z^2-r^2}$ energy, leading to an orbital polarization[9]. Based on the scenario of internal electrical field, the opposite electron transfer observed in the SIO_2/LNO_{10} bilayer, i.e., from Ni to Ir across the interface, may induce an opposite electric field that shortens the out-of-plane Ni–O bond and results in the observed opposite orbital polarization.

The change of Ni-O bond length modulates the *pd* hybridization, which can be evaluated by the XAS of O *K* pre-edge peak in perovskite nickelates[19,33]. The O *K* pre-edge peak corresponds to the transition from O 1*s* to the *pd* hybridized states. The full width of half maximum (FWHM) of the pre-edge peak is an indicator of the *pd* hybridization because a stronger overlap of the 3*d* and 2*p* states results in a broader distribution in energy of the hybridized states[19,33]. Figure 3c, d shows the O *K* pre-edge peak of SIO_2/NNO_{10} and SIO_2/LNO_{10}, respectively, normalized to the Ni L_3-edge[34]. Since Ir–O hybridization also contributes to the observed pre-edge peak, both pre-edge peaks of SIO_2/NNO_{10} and SIO_2/LNO_{10} bilayers are decomposed into Ni–O and Ir–O

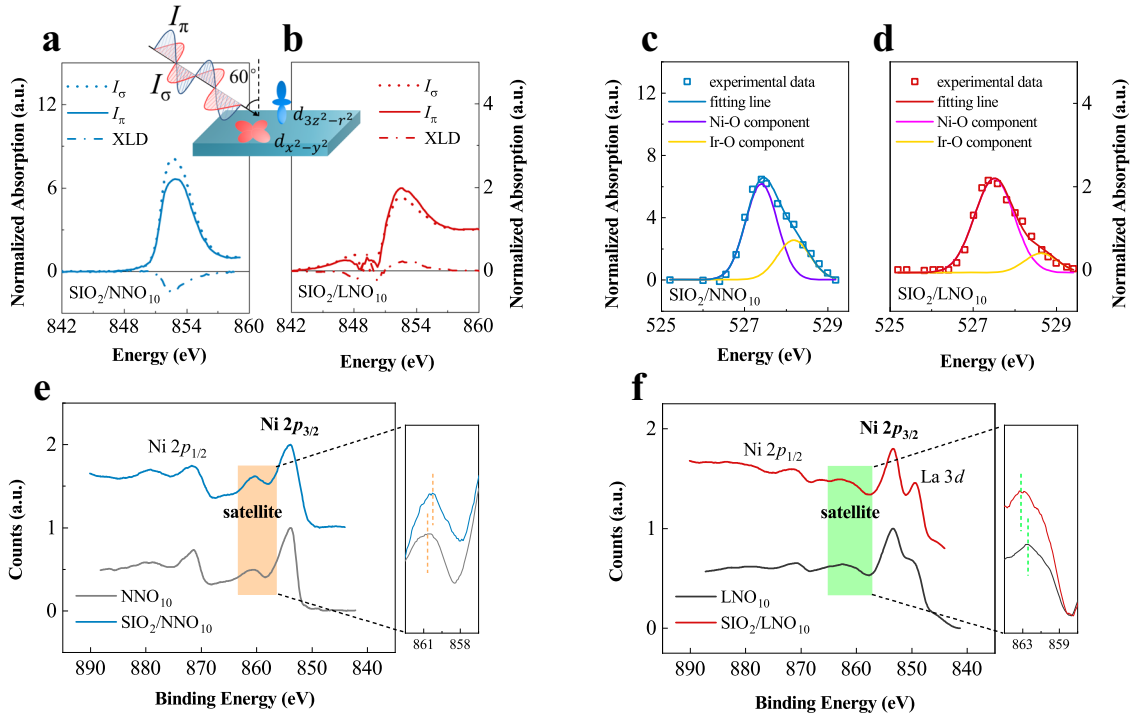

Fig. 3 Orbital polarization and *pd* hybridization. Ni L_3-edge X-ray absorption spectra (XAS) measured with the incident beam linearly polarized in (I_σ) or out (I_π) of the film plane and X-ray linear dichroism (XLD) spectra for **a** $(SrIrO_3)_2/(NdNiO_3)_{10}$ bilayer, abbreviated as SIO_2/NNO_{10}; and **b** $(SrIrO_3)_2/(LaNiO_3)_{10}$ bilayer, abbreviated as SIO_2/LNO_{10}, where I_σ, I_π and XLD represents by dotted, solid and dashed lines, respectively. The inset is a sketch of the measurement geometry. **c**, **d** are the Gaussian fitting of the O *K* pre-edge of SIO_2/NNO_{10} and SIO_2/LNO_{10} bilayers, respectively, where the purple and pink fitting lines represent the contribution from the Ni-O *pd* hybridization, and the yellow fitting line represents the contribution from the Ir-O *pd* hybridization, the blue and red open squares and lines represent the experimental data and cumulative fitting lines. **e**, **f** Ni 2*p* X-ray photoelectron spectra (XPS) of the SIO_2/NNO_{10} bilayer (blue line) in comparison with the NNO_{10} thin film (gray line), and the SIO_2/LNO_{10} bilayer (red line) in comparison with the LNO_{10} thin film (black line), respectively. The XPS of the bilayer is shifted to make the binding energy of Ni $2p_{3/2}$ of the thin film and bilayer as the same. The shaded Ni $2p_{3/2}$ satellite peaks are rescaled in the right panel to emphasize the shift of peak position, which are indicated by the orange and green dashed lines.

components[35]. In Fig. 3c, d, the peak at 528.2 eV and 528.6 eV can be assigned to the Ir-O contribution[36], while the peaks at 527.4 eV and 527.5 eV are from the Ni-O contribution[37]. The corresponding O *K* pre-edge peaks of NNO_{10} and LNO_{10} films are shown in Supplementary Fig. 4. The FWHM value of the Ni-O components in the O *K* pre-edge peak of SIO_2/NNO_{10}, NNO_{10}, SIO_2/LNO_{10} and LNO_{10} is 0.90, 0.98, 1.12 and 1.00 eV, respectively. The smaller FWHM in SIO_2/NNO_{10} and the larger FWHM in SIO_2/LNO_{10} suggest that the *pd* hybridization is stronger in SIO_2/LNO_{10}, but weaker in SIO_2/NNO_{10}.

XPS of Ni 2*p* core level can also be used to evaluate the *pd* hybridization[38]. It has been reported that in nickelates, the larger energy difference between Ni $2p_{3/2}$ and its satellite peak corresponds to a higher *pd* hybridization[37]. For example, Chen et al. observed that this energy difference is ~6.5 eV in NNO thin films[39], but ~9.0 eV in LNO thin films[40]. Figure 3e, f compares Ni 2*p* core level XPS of the SIO_2/NNO_{10} bilayer with the NNO_{10} thin film, and that of the SIO_2/LNO_{10} bilayer with the LNO_{10} thin film, respectively. The energy difference from Ni $2p_{3/2}$ to its satellite in NNO_{10} and LNO_{10} thin films is 6.7 and 9.2 eV, respectively, in agreement with values reported in the literature[39,40], indicating a higher degree of *pd* hybridization in LNO_{10} as expected. This energy difference in the SIO_2/NNO_{10} bilayer is 6.4 eV, smaller than that in the NNO_{10} thin film, while that in the SIO_2/LNO_{10} bilayer is 9.5 eV, larger than that in the LNO_{10} thin film. These suggest a decreased (increased) degree of *pd* hybridization in the SIO_2/NNO_{10} (SIO_2/LNO_{10}) bilayer, compared to the NNO_{10} (LNO_{10}) thin film, consistent with the XAS analysis.

Liu et al. have reported a transfer of electron from Ir to Ni in SIO/LNO superlattices and a preferential occupation of Ni $d_{x^2-y^2}$ orbital[15], which are opposite to the observations in our SIO_2/LNO_{10} heterostructures. We note that the SIO/LNO superlattices in Liu et al. work were deposited at 0.067 mbar oxygen pressure[15], much less than that used in the present work. Higher oxygen vacancy concentration may be expected in these samples. Malashevich et al. have studied the electronic structure of LNO with oxygen vacancies by first-principles calculations and found that the oxygen vacancies donate electrons into localized states below the Fermi level on the two nearest Ni cations of the vacancies[41]. The $d_{3z^2-r^2}$ orbitals on these two Ni cations form narrower bands and are at lower energies compared to the LNO in absence of oxygen vacancies[41]. This makes the electron transfer possible from SIO to oxygen deficient LNO. To check this, we deliberately studied a SIO_2/LNO_{10} bilayer sample without post-deposition annealing in oxygen. As shown in Fig. 2c, XPS results show that the Ir valence in the unannealed SIO_2/LNO_{10} bilayer is higher than that in SIO_{10} thin films. XAS and XLD results in Supplementary Fig. 5 show that the electron transfer direction and the orbital polarization of the unannealed sample are all opposite to the SIO_2/LNO_{10} sample post-annealed in oxygen, indicating the importance of oxygen vacancies in determining the electronic structure of perovskite nickelates, see Supplementary Discussion 1.

XLD of $[SIO_2/NNO_k]_l$ and $[SIO_2/LNO_k]_l$ superlattices, with multiple interfaces, are also studied. For the $[SIO_2/LNO_k]_l$ superlattices, XLD of Ni L_2-edge is used to avoid the disturbance of La M_4-edge that overlaps with the Ni L_3-edge. The sign of

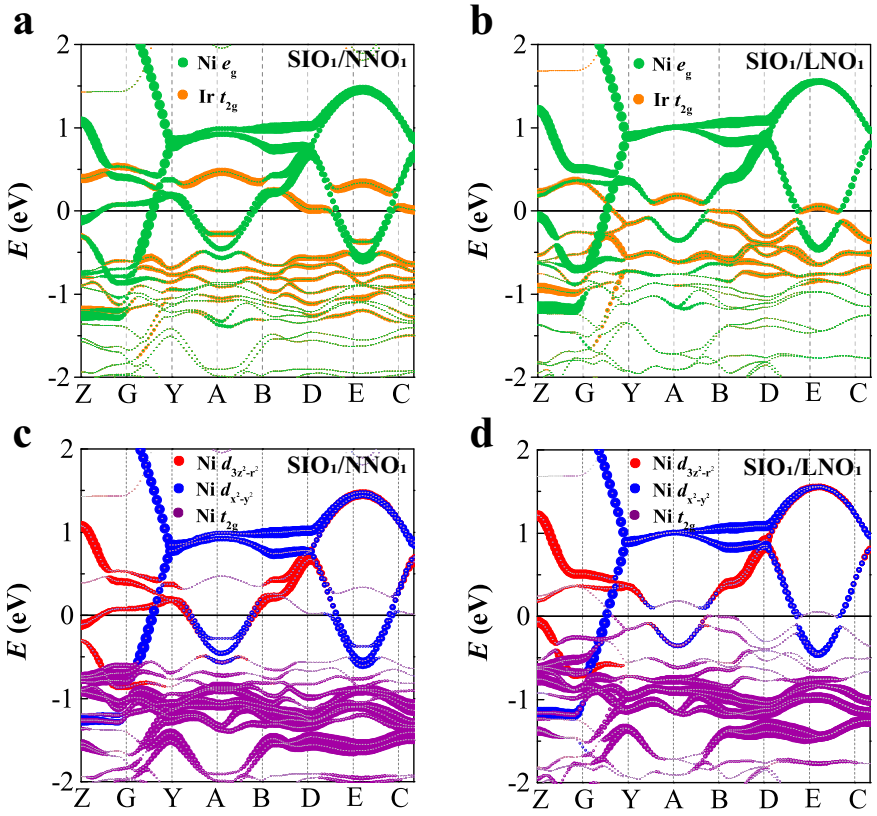

Fig. 4 Band structures and densities of states. Projected band structure of **a** $(SrIrO_3)_1/(NdNiO_3)_1$ (abbreviated as SIO_1/NNO_1), **b** $(SrIrO_3)_1/(LaNiO_3)_1$ (abbreviated as SIO_1/LNO_1) superlattices with Ni e_g orbitals and Ir t_{2g} orbitals are shown in green and orange. Projected band structure of **c** SIO_1/NNO_1, **d** SIO_1/LNO_1 superlattices with $d_{3z^2-r^2}$, $d_{x^2-y^2}$, t_{2g} of Ni 3*d* orbitals are shown in red, blue and purple, respectively. The fractional coordinate of Z, G, Y, A, B, D, E and C is (0,0,0.5), (0,0,0), (0,0.5,0), (0.5,0.5,0), (0.5,0,0), (0.5,0,0.5), (0.5,0.5,0.5), (0,0.5,0.5), respectively.

XLD, as shown in Supplementary Fig. 6, indicates that the Ni e_g electrons preferentially occupy the $d_{3z^2-r^2}$ ($d_{x^2-y^2}$) orbital in the $[SIO_2/NNO_k]_l$ ($[SIO_2/LNO_k]_l$) superlattices, i.e., exhibiting the same orbital polarization as observed in the corresponding bilayers, suggest the orbital polarization in superlattices could also be ascribed to the interfacial reconstruction.

First-principles calculations. First-principles calculations was carried out to further elucidate the electronic reconstruction of the $SrIrO_3/RNiO_3$ (R = La, Nd) superlattices. To be consistent with experiments, we fixed the in-plane lattice constants of the superlattices with the calculated lattice constants of STO (3.90 Å). Projected band structures of Ni e_g orbitals and Ir t_{2g} orbitals in SIO_1/NNO_1 and SIO_1/LNO_1 superlattices are shown in Fig. 4a, b. Across the fermi level, it can be observed that the Ni e_g orbitals in SIO_1/NNO_1 are obviously lower in energy than those in SIO_1/LNO_1, while the Ir t_{2g} orbitals in SIO_1/NNO_1 are higher in energy than those in SIO_1/LNO_1. These indicate that the Ni e_g orbitals are more occupied, but the Ir t_{2g} orbitals are less occupied in SIO_1/NNO_1 than in SIO_1/LNO_1. The electron transfer direction is consistent with those experimentally observed. By integrating the occupied states, electron transferred from Ni to Ir across the SIO_1/LNO_1 interface is estimated about 0.013 *e*/Ni, while that from Ir to Ni across the SIO_1/NNO_1 interface is about 0.007 *e*/Ni. Figure 4c, d shows projected band structures of $d_{3z^2-r^2}$, $d_{x^2-y^2}$, t_{2g} of Ni 3*d* orbitals in SIO_1/NNO_1 and SIO_1/LNO_1 superlattices. The Ni t_{2g} orbitals are almost fully occupied in both superlattices. Although the Ni $d_{x^2-y^2}$ orbitals do not change much in the two superlattices, the Ni $d_{3z^2-r^2}$ orbitals shift clearly upward in SIO_1/LNO_1 compared to those in SIO_1/NNO_1. There are more empty states in the $d_{3z^2-r^2}$ orbital of SIO_1/LNO_1 superlattice, in agreement with experimentally observed orbital polarization.

Interfacial lattice distortion. Figure 5a, b shows cross-sectional high angle annular dark field STEM (HAADF-STEM) images of the $[SIO_2/NNO_2]_6$ and $[SIO_2/LNO_2]_6$ superlattices, respectively. The intensity profiles along the [001] direction are obtained by averaging along the [010] direction in the area enclosed by the blue boxes. Clear distinctions between the HAADF-STEM intensity of different atomic layers suggest well controlled interfaces. From the intensity profiles, the average distance of two Ir atoms can be deduced as 3.97 Å and 4.00 Å, and that of two Ni atoms as 3.83 Å and 3.71 Å, respectively, in the $[SIO_2/NNO_2]_6$ and $[SIO_2/LNO_2]_6$ superlattices. Although the out-of-plane lattice parameter of the SIO_2 layer in these two superlattices are similar, the out-of-plane lattice parameter of the NNO_2 layer in $[SIO_2/NNO_2]_6$ is larger than that of the LNO_2 layer in $[SIO_2/LNO_2]_6$. Note that pseudo-cubic unit cell of NNO (3.81 Å) is smaller than that of LNO (3.86 Å) in bulk[42]. Chen and Mills pointed out that in perovskite oxide, the octahedron expands as an electron acceptor, but contracts as an electron donor[43]. The elongated (shortened) out-of-plane Ni-O bond in $[SIO_2/NNO_k]_l$ ($[SIO_2/LNO_k]_l$) superlattices can be understood taking into account the opposite electron transfer direction across these two iridate/nickelate interfaces. Figure 5c, d shows cross-sectional annular bright field STEM (ABF-STEM) images of the SIO_2/NNO_2 and SIO_2/LNO_2 interfaces, respectively. The interfacial out-of-plane Ni-O distance is extracted and plotted as a function of the horizontal unit cells number below the image. The averaged Ni–O distance of the $[SIO_2/NNO_2]_6$ superlattice (2.07 Å) is indeed

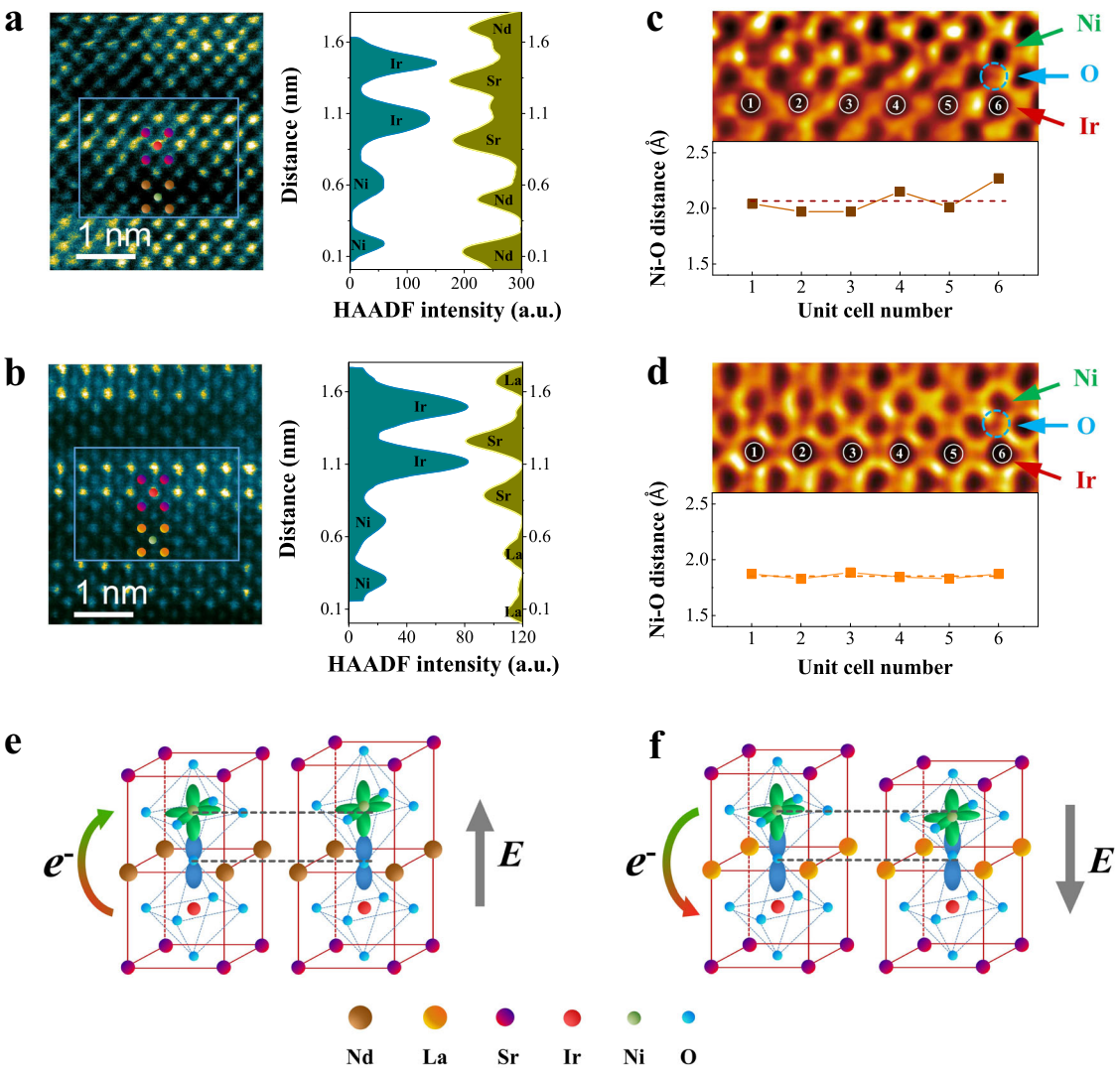

Fig. 5 Interfacial lattice distortion. Cross-sectional high angle annular dark field scanning transmission electron microscopy (HAADF-STEM) images of **a** $[(SrIrO_3)_2/(NdNiO_3)_2]_6$ and **b** $[(SrIrO_3)_2/(LaNiO_3)_2]_6$ superlattices and corresponding intensity profiles along the [001] direction extracted from the area enclosed by the blue boxes. Annular bright field scanning transmission electron microscopy (ABF-STEM) images of **c** $[(SrIrO_3)_2/(NdNiO_3)_2]_6$ and **d** $[(SrIrO_3)_2/(LaNiO_3)_2]_6$ superlattices, respectively. Interfacial out-of-plane Ni–O distance is plotted as functions of unit cell number under the corresponding image. Schematic lattice distortion at **e** $SrIrO_3/NdNiO_3$ and **f** $SrIrO_3/LaNiO_3$ interfaces before and after the electron transfer and the formation of internal electrical field *E*.

larger than that in the $[SIO_2/LNO_2]_6$ superlattice (1.85 Å), although the Ni–O distance of bulk NNO (1.942 Å) is similar to that of bulk LNO (1.935 Å)[42]. In the $[SIO_2/NNO_k]_l$ superlattice, the electron transferred from Ir to Ni would induce an electrical field pointing from Ir to Ni, driving down the apical O anions and stretching the Ni–O bonds at interface. However, in the $[SIO_2/LNO_k]_l$ superlattice, the opposite electron transfer results in an electric field pointing from Ni to Ir, driving up the apical O anions and compressing the Ni–O bonds[9]. This scenario is shown schematically in Fig. 5e, f for the $[SIO_2/NNO_k]_l$ and $[SIO_2/LNO_k]_l$ superlattices, respectively.

In ABO_3 perovskite oxides, intersite electron hopping and magnetic interactions are mediated through the overlap of B-site *d* orbitals with ligand O^{2-} *p* orbitals. Since both *d* and *p* orbitals are highly directional, subtle changes in B–O–B bond lengths and bond angles may alter the competition among charge, orbital and spin, leading to dramatic changes in transport and magnetic properties.

Transport characteristics. Figure 6a, b shows temperature-dependent resistivity (ρ-T) curves of the $[SIO_2/NNO_k]_l$ superlattices and NNO_k thin films, respectively. The $[SIO_2/NNO_6]_3$ and $[SIO_2/NNO_{10}]_2$ superlattices are metallic at high temperatures with a clear metal-insulator transition at a low temperature, while the $[SIO_2/NNO_4]_4$ and $[SIO_2/NNO_2]_6$ superlattices are insulating in the whole temperature range. Since the 2 u.c. SIO is insulating[44], the transport properties of the superlattices are dominated by the nickelate layers and the interfaces. Bulk NNO shows a structural transition in accompany with a metal-insulator transition at 201 K[42]. In rare earth perovskite nickelates, the metal-insulator transition temperature (T_{MIT}) increases rapidly with the decrease of *pd* hybridization[42]. Following Ojha et al., T_{MIT} can be determined as the temperature where $\frac{d\rho}{dT} = 0$[45], which are indicated in Fig. 6a, b. T_{MIT} of the $[SIO_2/NNO_6]_3$ and $[SIO_2/NNO_{10}]_2$ superlattices is 130 and 140 K, respectively, higher than 123 and 133 K of the corresponding NNO_6 and NNO_{10} thin films, suggesting the suppressed *pd* hybridization in the superlattices.

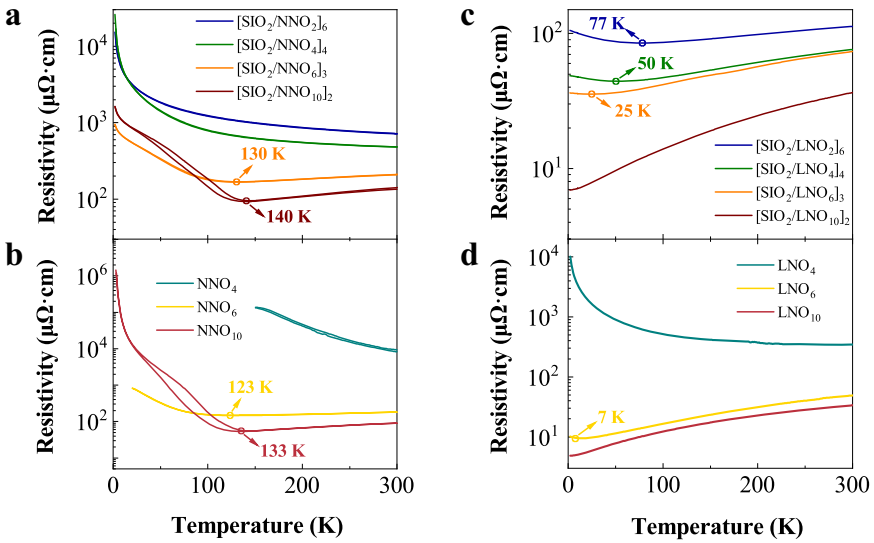

Fig. 6 Transport characteristics. Temperature dependent resistivity ($\rho - T$) curves of **a** the $[(SrIrO_3)_2/(NdNiO_3)_k]_l$ ($k = 2, 4, 6, 10$) superlattices, abbreviated as $[SIO_2/NNO_k]_l$, **b** the NNO_k ($k = 4, 6, 10$) films; **c** the $[(SrIrO_3)_2/(LaNiO_3)_k]_l$ ($k = 2, 4, 6, 10$) superlattices, abbreviated as $[SIO_2/LNO_k]_l$, and **d** the LNO_k ($k = 4, 6, 10$) films, where the $k = 2, 4, 6, 10$ superlattice samples are represented by blue, green, orange and brown, respectively and the $k = 4, 6, 10$ pure film samples are represented by cyan, yellow and red, respectively. The metal-insulator transition temperature is indicated by an open circle.

Figure 6c, d shows $\rho - T$ curves of the $[SIO_2/LNO_k]_l$ superlattices and LNO_k thin films, respectively. Bulk LNO is metallic, but insulating behavior and upturn of $\rho - T$ curve are often observed in ultrathin LNO films due to carrier localization, and the transition temperature T_{MIT} can be modulated by film thickness or epitaxial strain[46,47]. It is clear that the resistivity of both the $[SIO_2/LNO_k]_l$ superlattices and the LNO_k thin films increases with decreasing LNO thickness. The LNO_{10} film is metallic down to 2 K. The LNO_6 film shows an upturn of $\rho - T$ curve at 7 K. The LNO_4 film is insulating in the whole temperature range measured and the resistivity of the LNO_2 film is too large and out of the measurement range. The $[SIO_2/LNO_{10}]_2$ superlattice is also metallic similar to the LNO_{10} thin film. The other three $[SIO_2/LNO_k]_l$ superlattices are metallic at high temperature, but showing an upturn of $\rho - T$ curve at 25, 50 and 77 K, respectively, with $k = 6$, 4 and 2. The higher T_{MIT} in the $[SIO_2/LNO_6]_3$ superlattice, compared to that in the LNO_6 film, may be ascribed to the magnetic random scattering, as previously reported due to the existence of Ni^{4+} cations[17]. It is interesting that interfacing with the SIO_2 layer makes the otherwise insulating ultrathin LNO_4 and LNO_2 layers metallic at high temperature. The transport characteristics of the $[SIO_2/LNO_k]_l$ superlattices is very different from that of the LNO/$LaAlO_3$ superlattices, where the samples are insulating due to the strong localization by quantum confinement[48]. It is observed that T_{MIT} of the $[SIO_2/LNO_k]_l$ superlattices is independent of the magnetic field applied, as shown in Supplementary Fig. 7a, ruling out weak localization as the key component of the observed upturn of $\rho - T$ curve, because the insulating state due to the weak localization would be suppressed by the magnetic field[49]. The insulating part of the $\rho - T$ curve of the $[SIO_2/LNO_6]_3$ superlattice can be well fitted with the Kondo effect and three-dimensional weak localization, as shown in Supplementary Fig. 7b. Instead, the insulating part of $[SIO_2/LNO_4]_4$ and $[SIO_2/LNO_2]_6$ superlattices can be well fitted by the three-dimensional electron correlation model, as shown in Supplementary Fig. 7c, indicating the dominant role of electron–electron correlation, see Supplementary Discussion 2.

Taking into account the opposite lattice distortion due to the opposite electron transfer direction across the SIO/NNO and SIO/LNO interfaces, the transport characteristics of the $[SIO_2/NNO_k]_l$ and $[SIO_2/LNO_k]_l$ superlattices in comparison with their corresponding thin film counterparts can be well understood. In the $[SIO_2/NNO_k]_l$ superlattices, the elongated out-of-plane Ni-O bond and the suppressed *pd* hybridization facilitate the formation of the charge-transfer energy gap[42] and increase the T_{MIT}. This drives the $[SIO_2/NNO_k]_l$ superlattices into the insulating state at higher temperatures than the NNO_k thin films. Although metal-insulator transition in NNO might be more complex due to possible Ni-O bond disproportionate[50], the charge-transfer gap due to the suppressed *pd* hybridization in the superlattice may still be the dominant mechanism, as compared to the NNO_k thin films. In the $[SIO_2/LNO_k]_l$ superlattices, on the contrary, the compressed out-of-plane Ni–O bond and the enhanced *pd* hybridization increase the band width W and decrease the effective electron correlation U/W. This makes the $[SIO_2/LNO_k]_l$ superlattices more conductive than the LNO_k thin films.

Magnetic behavior. Figure 7a shows temperature-dependent magnetization (M-T) curves of the $[SIO_2/NNO_6]_3$ and $[SIO_2/LNO_6]_3$ superlattices, for example, compared to that of NNO_{10}, LNO_{10} and SIO_{10} thin film in Fig. 7b. The $[SIO_2/NNO_6]_3$ superlattice exhibit a paramagnetic-like behavior with small magnetizations increasing gradually with decreasing temperature, similar to the NNO_{10} film. The abrupt increase of magnetization at very low temperatures is due to the paramagnetic background from STO substrates[51]. Although NNO is an antiferromagnetic perovskite[52], the weak antiferromagnetic signal from Ni moments in NNO is hard to distinguish[53]. In contrast, the magnetization of the $[SIO_2/LNO_6]_3$ superlattice increases with decreasing temperature and saturates finally, showing a ferromagnetic-like behavior, different from the paramagnetic nature of its components LNO_{10} and SIO_{10}. The magnetization of $[SIO_2/LNO_k]_l$ superlattices is dependent on LNO layer thickness, as shown in Supplementary Fig. 8, suggesting that the observed magnetism in $[SIO_2/LNO_k]_l$ superlattices might originate from the LNO component, see Supplementary Discussion 3. Cho et al. reported that the appearance of Ni^{4+} cations with $d^8\underline{L}^2$ high-spin configuration could induce ferromagnetism or a spin glass state due to Ni^{4+}-O-

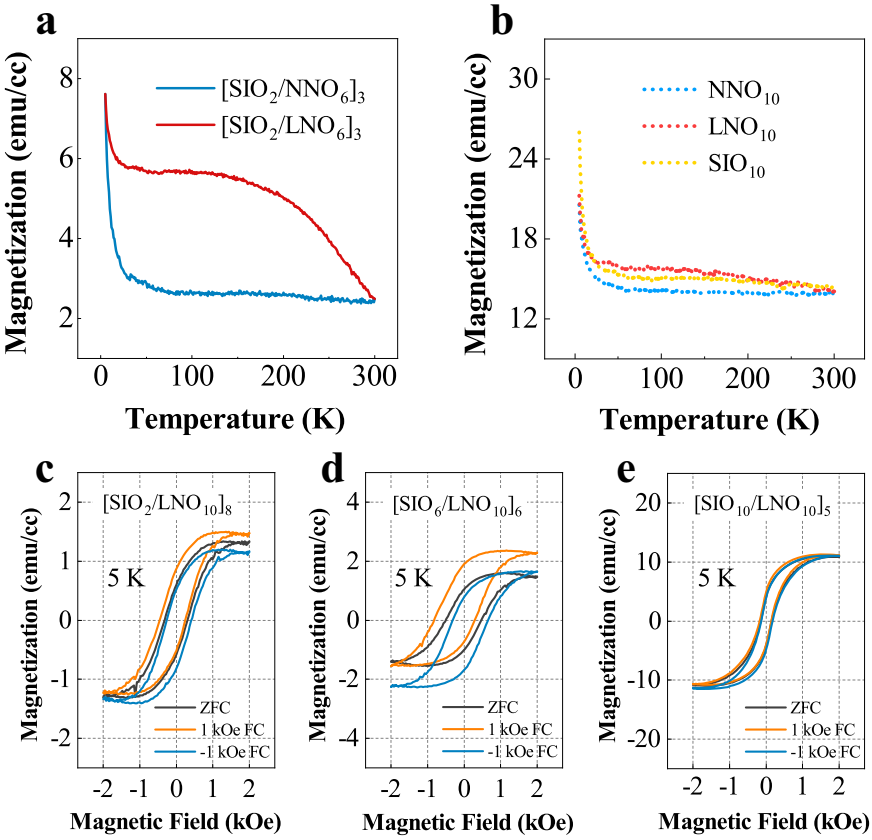

Fig. 7 Magnetic behaviors. a Temperature dependent magnetization (*M*-*T*) curves of the $[(SrIrO_3)_2/(NdNiO_3)_6]_3$ superlattice (blue line), abbreviated as $[SIO_2/NNO_6]_3$, and $[(SrIrO_3)_2/(LaNiO_3)_6]_3$ superlattice (red line), abbreviated as $[SIO_2/LNO_6]_3$ superlattice, measured with 1 kOe. **b** *M*-*T* curves of the NNO_{10} (blue dotted line), LNO_{10} (red dotted line) and SIO_{10} (yellow dotted line) thin films, measured with 1 kOe. In-plane field dependent magnetization (*M*-*H*) hysteresis loops of **c** $[SIO_2/LNO_{10}]_8$, **d** $[SIO_6/LNO_{10}]_6$ and **e** $[SIO_{10}/LNO_{10}]_5$ superlattice, respectively, measured at 5 K, after zero field cooling (ZFC) and field cooling (FC) with 1 and −1 kOe, which are represented by black, orange and blue lines, respectively.

Ni^{3+} double exchange interactions[54]. The differences of the magnetic behavior between $[SIO_2/NNO_6]_3$ and $[SIO_2/LNO_6]_3$ superlattices are ascribed to the different Ni valence states caused by the opposite interfacial electron transfer.

On the other hand, it has been reported that SIO layer thinner than 4 u.c. exhibits canted antiferromagnetic due to the interplay of spin-orbit coupling and electron correlation[55,56]. Exchange-bias is expected in ferromagnetic/antiferromagnetic heterostructures[57] and spin-glass/antiferromagnetic interface[58]. The field-dependent magnetization (*M*-*H*) loops of the $[SIO_2/LNO_{10}]_8$, $[SIO_6/LNO_{10}]_6$ and $[SIO_{10}/LNO_{10}]_5$ superlattices were measured at 5 K after cooling from 300 K with −1, 0, and 1 kOe magnetic field applied. As shown in Fig. 7c, d, an opposite vertical shift of the *M*-*H* loop is indeed observed in the $[SIO_2/LNO_{10}]_8$ and $[SIO_6/LNO_{10}]_6$ superlattices. Gruyters et al. has reported a vertical exchange-bias in CoO/Fe heterostructures[59] due to uncompensated spins at the ferromagnetic/antiferromagnetic interface[59,60]. Ferromagnetic or spin-glass state of LNO[17] in the superlattices may be pinned by the antiferromagnetic SIO, leading to the vertical shift of the hysteresis loops determined by the field direction during cooling[61,62]. However, SIO layers thicker than 4 u.c. are paramagnetic[55]. Exchange-bias should not be observed in $[SIO_6/LNO_{10}]_6$ and $[SIO_{10}/LNO_{10}]_5$ (Fig. 7e) superlattices. As the out-of-plane Ni-O bond shortens at the SIO/LNO interface, the corresponding Ir-O bond elongates, resulting in a smaller band width *W* and an enhanced effective electron correlation *U*/*W* in the SIO layer. This stronger electron correlation facilitates the antiferromagnetic coupling in the SIO layer, by altering the competition between electron correlation and spin-orbit coupling[63]. Therefore, the exchange-bias can be observed in the $[SIO_6/LNO_{10}]_6$ superlattice with a thicker SIO component. However, to further elucidate the appearance of these magnetic behavior requires the detection of Ir *L*-edge with a photon energy above 11 keV, which is not easy to access.

Conclusion

In summary, opposite electron transfer directions are observed in the SIO/NNO and SIO/LNO heterostructures, due to the different electronic structure in NNO and LNO, i.e., the lower Fermi level in NNO due to less *pd* hybridization. This opposite electron transfer results in an opposite e_g orbital polarization in Ni cations, by stretching (compressing) the out-of-plane Ni–O bonds in the SIO/NNO (SIO/LNO) heterostructures by the electron-transfer-induced opposite internal electric field. These structural and electronic reconstructions at the interface further suppress (enhance) the *pd* hybridization in the NNO and LNO layers and finally lead to modulations on transport and magnetic characteristics of the heterostructures, such as the increased T_{MIT} in the SIO/NNO heterostructures, and the enhanced conductivity, emerging ferromagnetism and exchange-bias in the SIO/LNO heterostructures. These results reveal the A site element in perovskite nickelates is a knob to control the electron transfer direction in iridate/nickelate heterostructures and the structural and electronic reconstructions at the 3*d*/5*d* perovskite interface may break the subtle balance among competing ground states to generate emerging phenomena that cannot be observed in bulk materials.

Methods

Sample preparation. SIO/NNO and SIO/LNO heterostructures, including bilayers and superlattices, were deposited on (001)-oriented $SrTiO_3$ substrates by pulsed laser deposition using a 248 nm KrF excimer laser (COMPex Pro 205 F, Coherent), monitored in situ by RHEED. The STO substrates were chemically treated and annealed in oxygen to achieve a single TiO_2-terminated step-terrace surface[64]. During the deposition, the substrate temperature was kept at 550 and 600 °C for SIO/NNO and SIO/LNO heterostructures, respectively, with the O_2 partial pressure kept at 0.1 mbar, the laser energy density at 1.8 J/cm^2 and the laser repetition at 2 Hz. In all the heterostructures, the first layer in direct contact with the STO substrates is always nickelates. The SIO layer was kept at 2 u.c. in thickness, while NNO and LNO layers vary from 2 to 10 u.c. in thickness. If not stated otherwise, samples were post-annealed in a tube furnace at their respective deposition temperature for 3 h in flowing O_2.

Sample characterization. XRD were performed using a Bruker D8 Discover diffractometer with Cu Kα radiation. Surface morphology of the samples were checked with an Asylum Research Cypher ES AFM. HAADF-STEM and ABF-STEM of the heterostructures were acquired using an aberration-corrected FEI Titan3 G2 microscope operating at 300 kV. Temperature-dependent resistivity were carried out in a physical property measurement system (PPMS-9, Quantum Design), through indium electrodes pressed on sample surface. Temperature-dependent magnetization and field-dependent magnetization were measured by a superconducting quantum interference device magnetometer (MPMS XL-7, Quantum Design). XPS was acquired with a Thermo Scientific K-Alpha spectrometer. XAS was collected at 300 K with total electron yield mode on beamline BL08U1A at Shanghai Synchrotron Radiation Facility, China.

Theoretical calculation. First-principles calculations were performed within density-functional theory, as implemented in the Vienna ab initio simulation package[65,66]. An energy cutoff of 550 eV was used, and the set of projector-augmented wave potentials was employed to describe the electron-ion interaction. Valence electron configurations, $4s^24p^65s^2$ for Sr, $5d^86s^1$ for Ir, $5s^25p^65d^16s^2$ for La, $3d^84s^2$ for Ni, $5s^25p^66s^2$ for Nd (the extra $4f$ electrons are frozen in the pseudopotentials) and $2s^22p^4$ for O were considered. Electronic relaxations converged within 10^{-7} eV and ionic relaxation converged within the force on each atom <1 meV Å^{-1} were performed in our calculations. We used the PBEsol + U[67] functional (selecting U = 2.5 eV for the Ir, U = 1 eV for Ni, note that the larger U for Ni in NNO would give similar results with U = 1 eV) for electronic structure calculations. A $\sqrt{2}\times\sqrt{2}\times 2$ supercell containing 20 atoms was used, and a Γ-centered $8\times8\times6$ k-point mesh was adopted.

Data availability

Data are available upon request from the authors.

Received: 26 February 2023; Accepted: 31 March 2023;
Published online: 14 April 2023

References

1. Ohtomo, A. & Hwang, H. Y. A high-mobility electron gas at the $LaAlO_3$/$SrTiO_3$ heterointerface. *Nature* **427**, 423–426 (2004).
2. Gibert, M., Zubko, P., Scherwitzl, R., Íñiguez, J. & Triscone, J. M. Exchange bias in $LaNiO_3$-$LaMnO_3$ superlattices. *Nat. Mater.* **11**, 195–198 (2012).
3. Sanchez-Manzano, D. et al. Extremely long-range, high-temperature Josephson coupling across a half-metallic ferromagnet. *Nat. Mater.* **21**, 188–194 (2022).
4. Chen, H. H. & Millis, A. Charge transfer driven emergent phenomena in oxide heterostructures. *J. Phys.: Condens. Matter* **29**, 243001 (2017).
5. Zhong, Z. C. & Hansmann, P. Band alignment and charge transfer in complex oxide interfaces. *Phys. Rev. X* **7**, 011023 (2017).
6. Chakhalian, J. et al. Orbital reconstruction and covalent bonding at an oxide interface. *Science* **318**, 1114–1117 (2007).
7. Cao, Y. W. et al. Engineered Mott ground state in a $LaTiO_{3+\delta}$/$LaNiO_3$ heterostructure. *Nat. Commun.* **7**, 10418 (2016).
8. Chen, H. H. et al. Modifying the electronic orbitals of nickelate heterostructures via structural distortions. *Phys. Rev. Lett.* **110**, 186402 (2013).
9. Disa, A. S. et al. Orbital engineering in symmetry-breaking polar heterostructures. *Phys. Rev. Lett.* **114**, 026801 (2015).
10. Hoffman, J. et al. Charge transfer and interfacial magnetism in $(LaNiO_3)_n$/$(LaMnO_3)_2$ superlattices. *Phys. Rev. B* **88**, 144411 (2013).
11. Fowlie, J. et al. Conductivity and local structure of $LaNiO_3$ thin films. *Adv. Mater.* **29**, 1605197 (2017).
12. Kumah, D. P. et al. Tuning the structure of nickelates to achieve two-dimensional electron conduction. *Adv. Mater.* **26**, 1935–1940 (2014).
13. Nelson, J. N. et al. Interfacial charge transfer and persistent metallicity of ultrathin $SrIrO_3$/$SrRuO_3$ heterostructures. *Sci. Adv.* **8**, eabj0481 (2022).
14. Nichols, J. et al. Emerging magnetism and anomalous Hall effect in iridate-manganite heterostructures. *Nat. Commun.* **7**, 12721 (2016).
15. Liu, X. R. et al. Interfacial charge-transfer Mott state in iridate-nickelate superlattices. *Proc. Natl Acad. Sci. USA* **116**, 19863–19868 (2019).
16. Wen, F. D. et al. Interface-engineered hole doping in Sr_2IrO_4/$LaNiO_3$ heterostructure. *N. J. Phys.* **21**, 103009 (2019).
17. Li, Y., Zhou, J. & Wu, D. Metal-insulator transition of $LaNiO_3$ films in $LaNiO_3$/$SrIrO_3$ heterostructures. *ACS Appl. Mater. Interfaces* **11**, 3565–3570 (2019).
18. Tung, I. C. et al. Connecting bulk symmetry and orbital polarization in strained $RNiO_3$ ultrathin films. *Phys. Rev. B* **88**, 205112 (2013).
19. Chakhalian, J. et al. Asymmetric orbital-lattice interactions in ultrathin correlated oxide films. *Phys. Rev. Lett.* **107**, 116805 (2011).
20. Freeland, J. W. et al. Orbital control in strained ultra-thin $LaNiO_3$/$LaAlO_3$ superlattices. *EPL* **96**, 57004 (2011).
21. Saleem, M. S. et al. Metal-insulator-metal transition in $NdNiO_3$ films capped by $CoFe_2O_4$. *Appl. Phys. Lett.* **110**, 072406 (2017).
22. Wang, L. et al. Hole-trapping-induced stabilization of Ni^{4+} in $SrNiO_3$/$LaFeO_3$ superlattices. *Adv. Mater.* **32**, 2005003 (2020).
23. Yamagami, K. et al. Local 3*d* electronic states of sulfur-coordinating Ni complexes probed by soft X-ray absorption spectroscopy. *Proc. Int. Conf. Strongly Correlated Electron Syst.* **30**, 011176 (2020).
24. Banerjee, W., Rahaman, S. Z. & Maikap, S. Excellent uniformity and multilevel operation in formation-free low power resistive switching memory using IrO_x/AlO_x/W cross-point. *Jpn. J. Appl. Phys.* **51**, 04DD10 (2012).
25. Chien, T. Y. et al. Visualizing short-range charge transfer at the interfaces between ferromagnetic and superconducting oxides. *Nat. Commun.* **4**, 2336 (2013).
26. Grisolia, M. N. et al. Hybridization-controlled charge transfer and induced magnetism at correlated oxide interfaces. *Nat. Phys.* **12**, 484–492 (2016).
27. García-Muñoz, J. L., Rodríguez-Carvajal, J., Lacorre, P. & Torrance, J. B. Neutron-diffraction study of $RNiO_3$ (R = La, Pr, Nd, Sm): electronically induced structural changes across the metal-insulator transition. *Phys. Rev. B* **46**, 4414 (1992).
28. Granados, X., Fontcuberta, J., Obradors, X., Mañosa, L. & Torrance, J. B. Metallic state and the metal-insulator transition of $NdNiO_3$. *Phys. Rev. B* **48**, 11666–11672 (1993).
29. Xu, X. Q., Peng, J. L., Li, Z. Y., Ju, H. L. & Greene, R. L. Resistivity, thermopower, and susceptibility of $RNiO_3$ (R=La, Pr). *Phys. Rev. B* **48**, 1112–1118 (1993).
30. Khomskii, D. I. Unusual valence, negative charge-transfer gaps and self-doping in transition-metal compounds. *Lithuanian J. Phys.* **37**, 65 (1997).
31. Thiel, S., Hammerl, G., Schmehl, A., Schneider, C. W. & Mannhart, J. Tunable quasi-two-dimensional electron gases in oxide heterostructures. *Science* **313**, 1942 (2006).
32. Pesquera, D. et al. Surface symmetry-breaking and strain effects on orbital occupancy in transition metal perovskite epitaxial films. *Nat. Commun.* **3**, 1189 (2012).
33. Liu, J. et al. Heterointerface engineered electronic and magnetic phases of $NdNiO_3$ thin films. *Nat. Commun.* **4**, 2714 (2013).
34. Disa, A. S. et al. Phase diagram of compressively strained nickelate thin films. *APL Mater.* **1**, 032110 (2013).
35. Roychoudhury, S. et al. Deciphering the oxygen absorption pre-edge: a caveat on its application for probing oxygen redox reactions in batteries. *Energy Environ. Mater.* **4**, 246–254 (2021).
36. Huang, W. C. et al. Enhanced orbital anisotropy through the proximity to a $SrTiO_3$ layer in the perovskite iridate superlattices. *Phys. Rev. B* **104**, 075156 (2021).
37. Chen, M. J. et al. The role of *pd* hybridization in the metal-insulator transition in $NdNiO_3$ heterostructure. *Mater. Res. Lett.* **6**, 515–521 (2018).
38. Zaanen, J., Westra, C. & Sawatzky, G. A. Determination of the electronic structure of transition-metal compounds: 2*p* x-ray photoemission spectroscopy of the nickel dihalides. *Phys. Rev. B* **33**, 8060–8073 (1986).
39. Chen, M. J. et al. Interfacial e_g orbital reconstruction: modulation of metal-insulator transitions of ultrathin $NdNiO_3$ films by two-dimensional electronic gas. *Phys. B* **612**, 412744 (2021).
40. Chen, M. J. et al. Polarization and charge-transfer effect on the transport properties in two-dimensional electron gases/$LaNiO_3$ heterostructure. *Appl. Phys. Lett.* **112**, 021601 (2018).
41. Malashevich, A. & Ismail-Beigi, S. First-principles study of oxygen-deficient $LaNiO_3$ structures. *Phys. Rev. B* **92**, 144102 (2015).
42. Medarde, M. L. Structural, magnetic and electronic properties of $RNiO_3$ perovskites. *J. Phys. Condens. Matter* **9**, 1679–1707 (1999).
43. Chen, H. & Millis, A. Antisite defects at oxide interfaces. *Phys. Rev. B* **93**, 104111 (2016).

44. Groenendijk, D. J. et al. Spin-orbit semimetal $SrIrO_3$ in the two-dimensional limit. *Phys. Rev. Lett.* **119**, 256403 (2017).
45. Ojha, S. K. et al. Anomalous electron transport in epitaxial $NdNiO_3$ films. *Phys. Rev. B* **99**, 235153 (2019).
46. Son, J. et al. Low-dimensional Mott material: transport in ultrathin epitaxial $LaNiO_3$ films. *Appl. Phys. Lett.* **96**, 062114 (2010).
47. Scherwitzl, R. et al. Metal-insulator transition in ultrathin $LaNiO_3$ films. *Phys. Rev. Lett.* **106**, 246403 (2011).
48. Liu, J. et al. Quantum confinement of Mott electrons in ultrathin $LaNiO_3$/$LaAlO_3$ superlattices. *Phys. Rev. B* **83**, 161102 (2011).
49. Xu, Y., Zhang, J. C., Cao, G. X., Jing, C. & Cao, S. X. Low-temperature resistivity minimum and weak spin disorder of polycrystalline $La_{2/3}Ca_{1/3}MnO_3$ in a magnetic field. *Phys. Rev. B* **73**, 224410 (2006).
50. Mazin, I. I. et al. Charge ordering as alternative to Jahn-Teller distortion. *Phys. Rev. Lett.* **98**, 176406 (2007).
51. Khalid, M. et al. Ubiquity of ferromagnetic signals in common diamagnetic oxide crystals. *Phys. Rev. B* **81**, 214414 (2010).
52. Scagnoli, V. et al. Role of magnetic and orbital ordering at the metal-insulator transition in $NdNiO_3$. *Phys. Rev. B* **73**, 100409 (2007).
53. Kumar, D., Rajeev, K. P., Alonso, J. A. & Martínez-Lope, M. J. Spin-canted magnetism and decoupling of charge and spin ordering in $NdNiO_3$. *Phys. Rev. B* **88**, 014410 (2013).
54. Cho, E. et al. First-principles calculation of oxygen vacancy effects on the magnetic properties of the perovskite $SrNiO_3$. *Phys. Rev. Mater.* **5**, 094413 (2021).
55. Matsuno, J. et al. Engineering a spin-orbital magnetic insulator by tailoring superlattices. *Phys. Rev. Lett.* **114**, 247209 (2015).
56. Yang, J. Y. et al. Strain-modulated Slater-Mott crossover of pseudospin-half square-lattice in $(SrIrO_3)_1/(SrTiO_3)_1$ superlattices. *Phys. Rev. Lett.* **124**, 177601 (2020).
57. Nogués, J. & Schuller, I. K. Exchange bias. *J. Magn. Magn. Mater.* **192**, 203–232 (1999).
58. Mannan, A. et al. Exchange bias using a spin glass. *Nat. Mater.* **6**, 70–75 (2007).
59. Gruyters, M. & Schmitz, D. Microscopic nature of ferro- and antiferromagnetic interface coupling of uncompensated magnetic moments in exchange bias systems. *Phys. Rev. Lett.* **100**, 077205 (2008).
60. Ohldag, H. et al. Correlation between exchange bias and pinned interfacial spins. *Phys. Rev. Lett.* **91**, 017203 (2003).
61. Nogués, J., Leighton, C. & Schuller, I. K. Correlation between antiferromagnetic interface coupling and positive exchange bias. *Phys. Rev. B* **61**, 1315 (2000).
62. Gruyters, M. Spin-glass-like behavior in CoO nanoparticles and the origin of exchange bias in layered CoO/ferromagnet structures. *Phys. Rev. Lett.* **95**, 077204 (2005).
63. Zeb, M. A. & Kee, H. Y. Interplay between spin-orbit coupling and Hubbard interaction in $SrIrO_3$ and related *Pbnm* perovskite oxides. *Phys. Rev. B* **86**, 085149 (2012).
64. Koster, G., Kropman, B. L., Rijnders, G. J. H. M., Blank, D. H. A. & Rogalla, H. Quasi-ideal strontium titanate crystal surfaces through formation of strontium hydroxide. *Appl. Phys. Lett.* **73**, 2920 (1998).
65. Kresse, G. & Furthmüller, J. Efficient iterative schemes for ab initio total-energy calculations using a plane-wave basis set. *Phys. Rev. B* **54**, 11169 (1996).
66. Kresse, G. & Hafner, J. Ab initio molecular dynamics for liquid metals. *Phys. Rev. B* **47**, 558 (1993).
67. Perdew, J. P. et al. Restoring the density-gradient expansion for exchange in solids and surfaces. *Phys. Rev. Lett.* **100**, 136406 (2008).

Acknowledgements

This work was jointly sponsored by Natural Science Foundation of China (grant Nos. 51725203, U1932115, 51721001, and 52003117). Shanghai Synchrotron Radiation Facility is greatly acknowledged for providing the beam time and technical assistance.

Author contributions

D.W. conceived this work. Y.L. deposited the heterostructures and measured the structural, transport and magnetic properties with the help of P.X.H., Z.N.X., and J.Y.L.; collected the XAS data with the help of P.X.H. and Y.M.X.; J.Y.L. and Y.D. take the STEM measurements; Y.R.L. and H.T. carried out the first-principles calculations; Y.L. and D.W. analyzed the data with the help of Y.D. and Y.R.Y.; Y.L. and D.W. wrote the manuscript.

Competing interests

The authors declare no competing interests.

Additional information

Supplementary information The online version contains supplementary material available at https://doi.org/10.1038/s42005-023-01194-0.

Correspondence and requests for materials should be addressed to Yurong Yang or Di Wu.

Peer review information *Communications Physics* thanks the anonymous reviewers for their contribution to the peer review of this work.

Reprints and permission information is available at http://www.nature.com/reprints

Publisher's note Springer Nature remains neutral with regard to jurisdictional claims in published maps and institutional affiliations.